ADVANCED ELECTRONIC MATERIALS Open Access
www.advelectronicmat.de

n-Type GaSe Thin Flake for Field Effect Transistor, Photodetector, and Optoelectronic Memory

Arun Kumar, Aniello Pelella, Kimberly Intonti, Loredana Viscardi, Ofelia Durante, Filippo Giubileo, Paola Romano, Hazel Neill, Vilas Patil, Lida Ansari, Paul K. Hurley, Farzan Gity, and Antonio Di Bartolomeo**

The family of 2D chalcogenide semiconductors has been growing rapidly. Metal monochalcogenides, for instance, can enable new possibilities in functional electronics and optoelectronics. A Gallium Selenide (GaSe) thin flake is used to fabricate a back gated field effect transistor (FET) with n-type conduction behavior and wide hysteresis at the ambient conditions. The device shows high mobility up to 28 $cm^2\ V^{-1}\ s^{-1}$ with I_{on}/I_{off} ratio over 10^3. Under the laser exposure, the device shows a decrease in the threshold voltage and a left-shift of the transfer characteristic with a slight increase in the current. The transfer characteristic exhibits a hysteretic behavior with hysteresis width linearly dependent on the applied gate voltage. Moreover, the GaSe-based FET shows a photo response with a photoresponsivity of 475 mAW^{-1} and detectivity of 4.6×10^{12} Jones. The photocurrent rise and decay times are 0.1 and 1.3 s, respectively. Furthermore, the GaSe FET device can be used as a performant memory device with well separated states and memory window enhanced by the laser exposure, confirming an optoelectronic memory class.

1. Introduction

Over the last decade, there has been a significant rise in research efforts dedicated to 2D materials, such as graphene and transition metal dichalcogenides (TMDCs).[1–4] The period has witnessed remarkable advancements in both fundamental understanding and applications.[5–11] These 2D materials have captured attention due to their intriguing properties and their potential for future electronic and optoelectronic technologies. Among these 2D materials, graphene stands out as one of the most critical candidates for nanoelectronics. However, the inherent zero bandgap restricts its use in applications involving logic electronics and field-effect transistors (FETs). On the other hand, TMDCs like MoS_2, $MoSe_2$, WS_2, WSe_2, $PtSe_2$, $ReSe_2$, ReS_2, etc. and black phosphorus (BP) have successfully addressed the zero-bandgap constraint of graphene, demonstrating remarkable capabilities as FETs,[12–14] photodetectors,[12,15–17] optoelectronic memories,[18–21] and sensors.[22,23]

In the most recent developments, atomically thin metal monochalcogenides like GaSe, GaS, GeAs, and InSe have been extensively studied.[24–28] These materials exhibit substantially distinct electronic and optoelectronic properties when compared to TMDCs. Unlike the TMDCs, these materials possess a direct bandgap in the bulk form, and show indirect bandgap in the single-layer form.[29] In the class of metal monochalcogenides, GaSe is a semiconducting material falling within the III–VI group. In the multi-layer configuration, GaSe has a direct bandgap of ≈2 eV which makes it a suitable material for photodetection and optoelectronic memory applications.[30] However, when thinned to a monolayer, the GaSe bandgap becomes indirect and widens to ≈4 eV.[31] The material is made of layers, each consisting of a distinct sequence of four atoms: Se–Ga–Ga–Se. These layers are bound together by a relatively weak van der Waals force, which facilitates their separation through mechanical exfoliation.[32] Few-layered 2D GaSe has showcased interesting electrical and optical characteristics, such as p-type conduction behavior,[33] high hall mobility,[34] high current on-off ratio,[35] photoresponsivity,[33,36] and gas sensitivity.[37,38]

A. Kumar, K. Intonti, L. Viscardi, O. Durante, A. Di Bartolomeo
Department of Physics "E. R. Caianiello"
University of Salerno
via Giovanni Paolo II n. 132, Fisciano 84084, Salerno, Italy
E-mail: akumar@unisa.it; adibartolomeo@unisa.it

A. Pelella, P. Romano
Department of Science and Technology
University of Sannio
Via de Sanctis, Benevento 82100, Italy

F. Giubileo
CNR-SPIN Salerno
via Giovanni Paolo II n. 132, Fisciano 84084, Salerno, Italy

H. Neill, V. Patil, L. Ansari, P. K. Hurley, F. Gity
Tyndall National Institute
University College Cork
Lee Maltings, Dyke Parade, Cork T12 R5CP, Ireland

P. K. Hurley
School of Chemistry, University College Cork
Cork Ireland

The ORCID identification number(s) for the author(s) of this article can be found under https://doi.org/10.1002/aelm.202400010

DOI: 10.1002/aelm.202400010

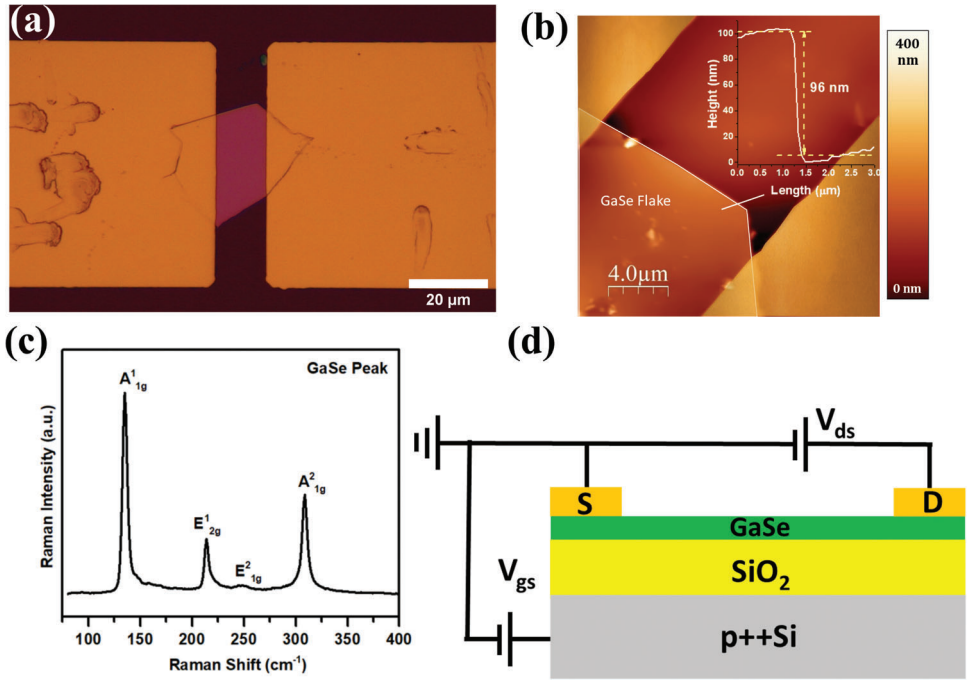

Figure 1. a) Optical image, b) AFM image and height profile, c) Raman spectrum of the exfoliated GaSe flake, and d) Schematic of the back-gate FET with a GaSe flake as the channel, metal leads as the source and drain, and the Si substrate as the common back-gate.

As initial demonstrations on the 2D GaSe have shown promising results, numerous challenges such as large area growth, low operating voltages, stability, etcetera remain on the path toward creating dependable devices compatible with existing silicon technologies. Moreover, the majority of GaSe transistors reported in existing literature exhibit p-type electrical transport characteristics. Conversely, reports about n-type conduction response of GaSe-based transistors are scarce, which not only constrains the fundamental understanding but also hinders the widespread incorporation of GaSe into technological applications, notably in complementary metal-oxide semiconductor circuits to achieve low power consumption and high performance.

In the present work, we report on the fabrication and characterization of a back gated GaSe thin flake mechanically exfoliated over SiO_2/Si substrate. The GaSe flake channel is about 100 nm thick and about 300 μm^2 in area. The electrical characteristics of the back gated GaSe FET show a n-type conduction at ambient conditions with high mobility and I_{on}/I_{off} ratio. Our first-principles calculations demonstrate asymmetric band offset between the Ni contact and the GaSe channel explaining the n-type response of the FET device. The GaSe device is thoroughly investigated as a FET and as a photodetector. Typical figures of merits are extracted from the experimental data. Furthermore, the device is explored for optoelectronic memory applications, showing stable memory behavior for more than 1 h and enhanced programming window under laser exposure. The role of trap states and adsorbates such as oxygen (O_2) and water (H_2O) molecules onto the surface of GaSe has been discussed in detail. We believe that this work provides a first report on the n-type conduction behavior of thin GaSe flake as well as the reported benchmarking optoelectrical characteristics that open the path for integrating such materials in optoelectronic devices.

2. Results and Discussion

GaSe thin flakes were mechanically exfoliated from GaSe single crystals by a scotch tape method. **Figure** 1a shows a typical optical image of the exfoliated GaSe fabricated device on the silicon substrate with 300 nm thick SiO_2. The 15/150 nm Ni/Au metal contacts over the GaSe flake were defined by the lithography process. The thickness of the exfoliated GaSe flake was measured by atomic force microscopy (AFM). Figure 1b shows the AFM image and height profile of the GaSe flake. The measured thickness of the GaSe flake was ≈100 nm. Raman spectroscopy is a powerful characterization technique for understanding the electronic structure and interaction of layered semiconductor materials. In Figure 1c, we present the Raman spectrum of a single GaSe bulk flake. The Raman scattering peaks of the GaSe flake are located at ≈135, 214, 245, and 309 cm^{-1}, corresponding to the $A^1{}_{1g}$, $E^1{}_{2g}$, $E^2{}_{1g}$, and $A^2{}_{1g}$ vibration modes, respectively. The Raman peaks are consistent with the data reported in the literature.[39–41] The A_{1g} peaks with the highest intensity are the result of vibrations occurring out-of-plane, whereas the remaining peaks are the result of vibrations occurring in the crystal plane. Figure 1d presents a schematic cross-sectional view of a back gated GaSe FET with its electrical connections.

Figure 2a shows the output characteristics on a linear scale of the fabricated GaSe FET device performed at different gate voltages, V_{gs}, ranging from −50 to +50 V. The device confirms the current modulation by the applied gate voltage. A decrease in the channel current at the negative gate bias shows that the device exhibits n-type conduction. At negative V_{gs}, the current is very low, meaning that the transistor is in the off state. At $V_{gs} > 0$ V, the device is in the on state and the source-drain current (I_d) presents a slight rectification for positive and negative source-drain

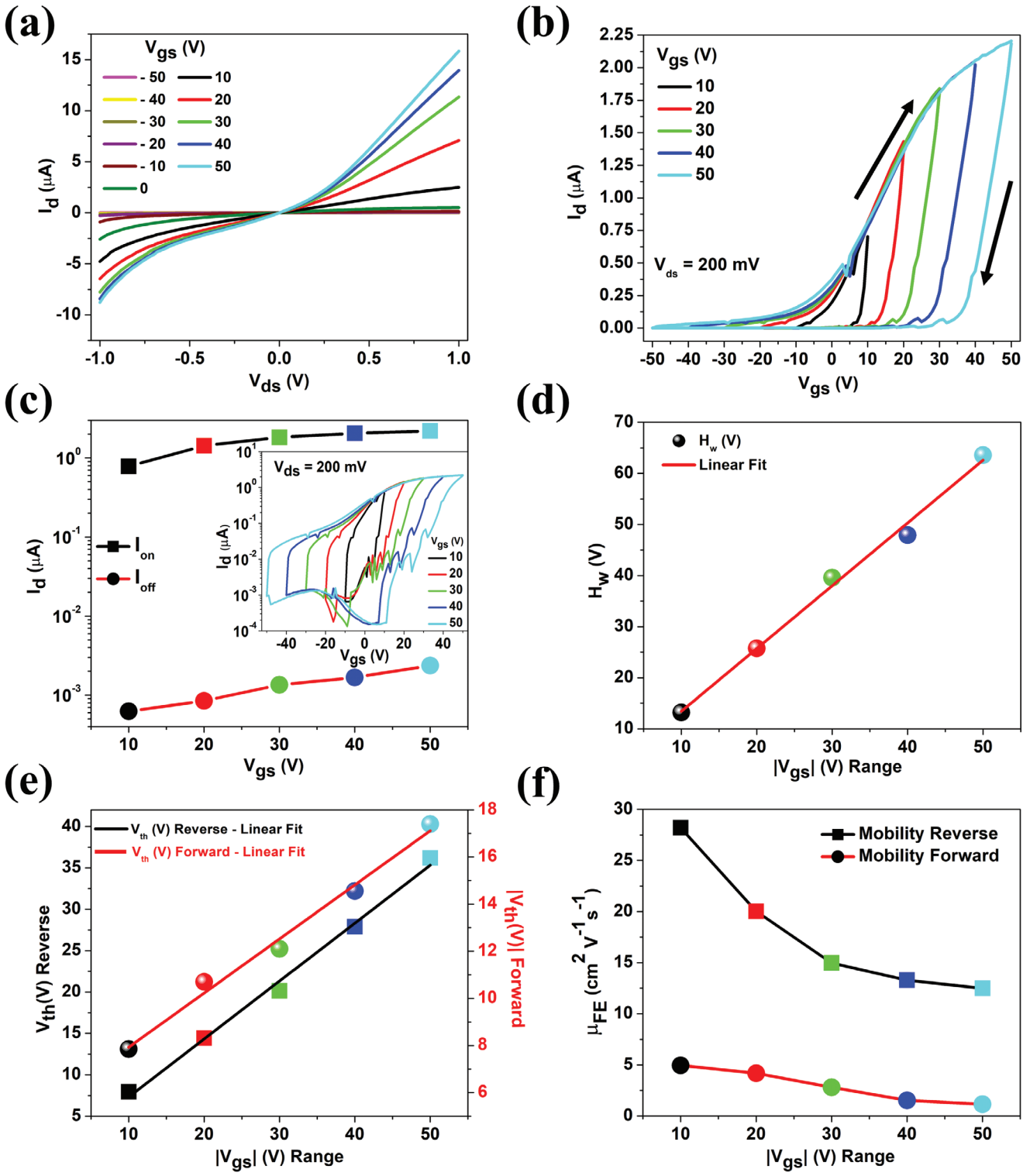

Figure 2. a) Output, b) transfer characteristics of the fabricated GaSe device on a linear scale, c) I_{on} and I_{off} current as a function of V_{gs}, respectively (inset: transfer curves on a log scale), d) calculated hysteresis width of the transfer characteristics, e) threshold voltage from the forward and reverse sweep curves, and f) field effect mobility as a function of the gate voltage range.

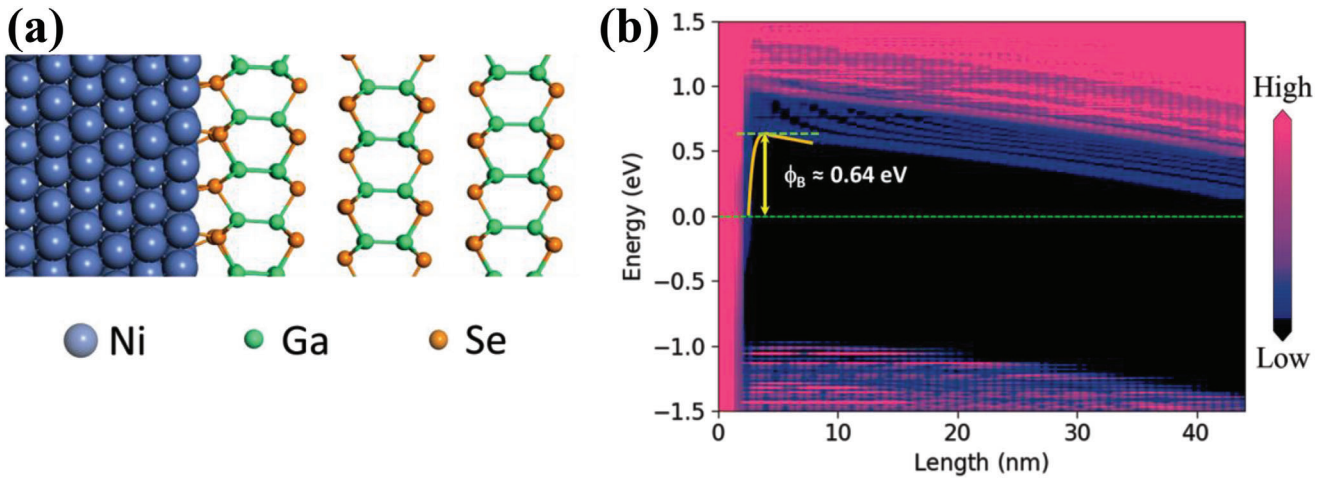

Figure 3. a) Atomic structure of Ni–GaSe interface, and b) LDoS of the Ni–GaSe junction, demonstrating the asymmetric conduction band and valence band offsets at the interface.

voltage (V_{ds}). This behavior indicates the presence of a Schottky barrier (SB) at the GaSe/Ni interface.[42,43] Due to the formation of interfacial chemical bonding between metal and Se, the bottom Se sublayer is distorted, giving a vertical buckling causing SB height.[44] We note that it has been reported that the SB height decreases as the thickness of GaSe flake increases so a SB is expected also with thinner GaSe flakes.[45]

To explore the gate control effect on the device and confirm the n-type conduction, the transfer characteristic (I_d–V_{gs}) was recorded at different V_{ds} at ambient conditions. Figure 2b represents the transfer characteristics of the back-gated FET under a drain bias of 200 mV at different loops of the applied gate voltages up to $V_{gs} = \pm 50$ V, in a clockwise direction. The I_d values were measured by sweeping V_{gs} from negative to positive and back to negative, and a closed clockwise hysteresis loop was obtained. Although limited by the thickness of the flake, the back-gated FET showed good gate control capability with I_{on}/I_{off} ratio higher than 10^3 (see Figure 2c). The transfer characteristics confirm the n-type conduction behavior, indicating that the Fermi level of the fabricated GaSe transistor with Ni contacts is closer to the conduction band of GaSe. The measurements in the ± 50 V range do not show any ambipolar behavior, but rather a strong unipolar n-type conduction behavior due to the asymmetric band offset. The hysteresis loop can be attributed to the intrinsic traps in the GaSe and the GaSe–SiO_2 interface defects as well as to surface adsorbates such as O_2 and H_2O molecules.[46–50]

Figure 2d demonstrates that the hysteresis width (H_w), defined as the V_{gs} difference corresponding to the average current $I_m = (I_{on} + I_{off})/2$ between the highest (I_{on}) and lowest (I_{off}) currents at the extreme of the gate voltage range is a linear function of V_{gs}. The increase in the hysteresis width with V_{gs} sweep range is attributed to a larger density of charges being trapped in the intrinsic and extrinsic trap states of the material at higher bias voltages. As the measurements were carried out at ambient conditions, the adsorbates on the GaSe surface contribute to the enhancement of hysteresis. Likewise, threshold voltage from the reverse sweep shows a linear increase with the applied gate voltage range (see Figure 2e). The right-shift of the transfer characteristic during the reverse sweep indicates that negative charges are trapped and cause hysteresis. Similarly, a decreasing threshold voltage (see inset of Figure 2c) is observed during the forward sweep due to the storage of positive charge.

The following equation was used for calculating the field effect charge carrier mobility of the GaSe FET from the transfer characteristic measured during the reverse and forward sweeps:

$$\mu_{FE} = \frac{L}{WC_{ox}V_{ds}} \frac{dI_d}{dV_{gs}} \quad (1)$$

where, $L = 13.3$ μm, $W = 22.5$ μm, $C_{ox} = 4.06 \times 10^{-8}$ Fcm^{-2}, and dI_d/dV_{gs} are the channel length, channel width, gate oxide capacitance, and the slope over the linear region of the transfer curve, respectively. We inferred two-terminal field-effect mobilities (see Figure 2f), in the reverse and forward bias direction, with maximum values of 28 and 5 cm^2 V^{-1} s^{-1} at $V_{ds} = 200$ mV, respectively. The calculated field effect mobility is much higher than previously reported values for p-type GaSe.[51–54] The different mobilities in the two directions and the dependence on V_{gs} can be ascribed to the deep trap states which are differently populated under different bias sweeps. We also note that the mobility reduces with enhanced V_{gs} sweep range. This is attributed to the interfacial or surface defects, where the increased electric field can influence charge trapping. Trapped charges can introduce localized potential fluctuations that hinder the movement of charge carriers, reducing mobility. It should be remarked that 2D thin GaSe shows lower mobility than bulk GaSe with reported Hall mobilities up to 215 cm^2 V^{-1} s^{-1}.[34,55] Hence, it would be promising to produce GaSe nanosheets over a large area with comparably high mobility, suitable for the fabrication of semiconductor devices.

The local density of states (LDoS) can indicate the SB height at the metal–semiconductor interface.[56] Our first-principles calculations reveal that the GaSe conduction and valence bands bend upwards to near the interface with Ni. **Figure 3a** shows the atomic structure of the Ni/GaSe interface. From Figure 3b, it can be seen that at distances larger than approximately 25 nm into the GaSe semiconducting region, the band bending measured in the conduction band is +0.35 eV, while the conduction and valence band offsets at the interface with Ni are ≈0.64 and ≈1.4 eV, respectively.

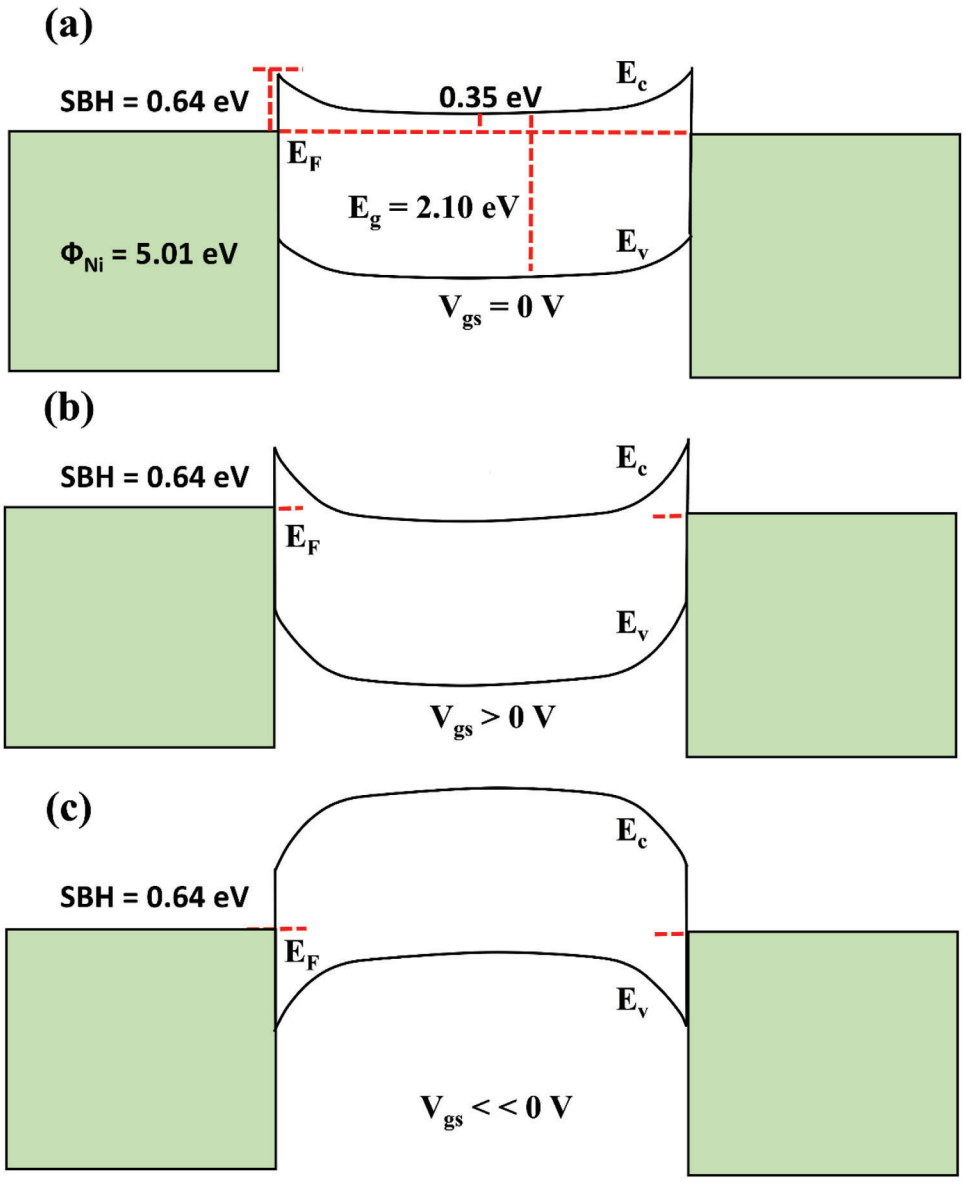

Figure 4. Energy band alignment in a GaSe FET at $V_{ds} > 0$V: a) with $V_{gs} = 0$ V, b) at $V_{gs} > 0$ V, and c) at $V_{gs} \ll 0$ V.

The investigated GaSe thin flake exhibits n-type conduction, mainly due to the band offset. The output behavior of the device, and the density functional theory (DFT) calculations are described in **Figure 4**. Figure 4 represents the energy band diagrams of GaSe along the vertical axis showing the Ni/GaSe contact, at different V_{gs}. According to the DFT calculations, the Ni/GaSe interface forms an SB height of 0.64 eV. At $V_{gs} = 0$ V, when no bias is applied the conduction and valence band edges of GaSe and the metal electrode Fermi levels are aligned as in Figure 4a, showing the formation of an SB. However, when applying $V_{gs} > 0$ V, the GaSe conduction band moves downwards to Fermi level and favors the flow of electrons across the channel, forming the n-type GaSe (see Figure 4b). Conversely, the negatively increasing V_{gs} makes the bands bend upward, switching the current between the source and drain off (see Figure 4c).

Figure 5a,b shows the transfer curves of the GaSe device with V_{ds} ranging from 100 to 1000 mV, on linear and log scales, respectively. As can be seen in Figure 5c, I_{on} is linearly dependent on V_{ds}, confirming the device in the linear (triode) region over the investigated V_{gs} and V_{ds} voltages. Further, as shown in Figure 5d, a decreasing trend of the hysteresis width of the transfer characteristics has been observed as a function of increasing V_{ds}. Such a trend points towards the role of the intrinsic traps in the GaSe channel, which add to the ones present at the GaSe–SiO_2 interface in the generation of hysteretic behavior. It can be noted that lower V_{ds} facilitates the charge trapping in the GaSe channel and results in wider hysteresis.[12]

Further, the photo response of the GaSe FET device was carried out under the white laser illumination. The multilayer GaSe flake ensures higher light absorption with respect to the monolayer or

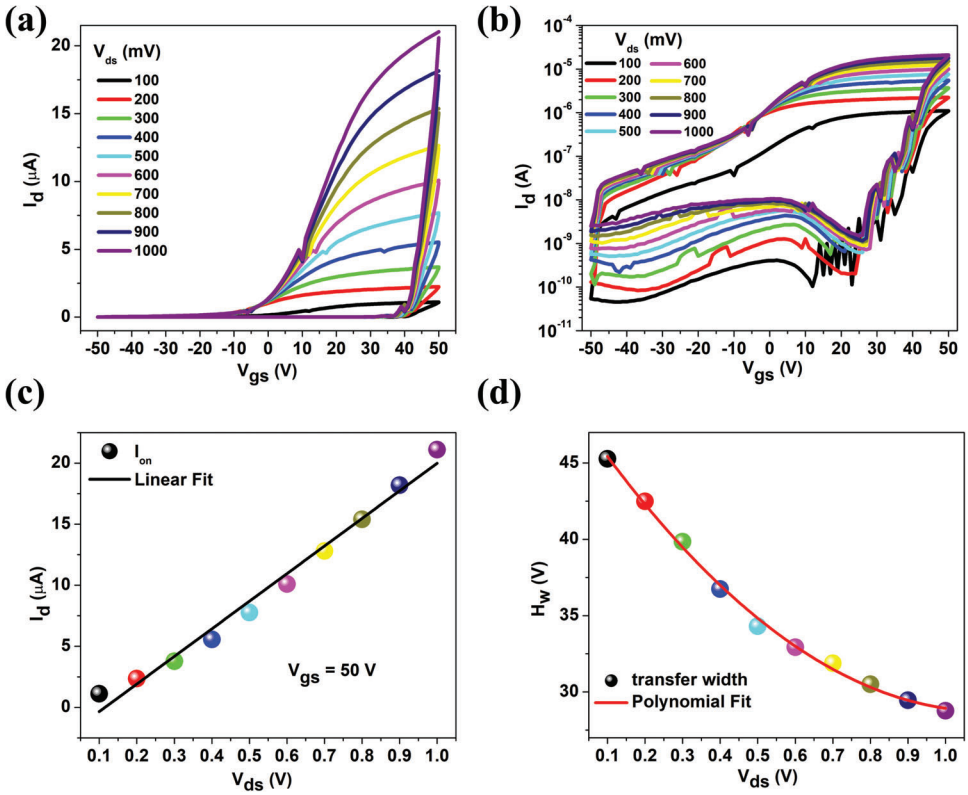

Figure 5. a,b) Transfer characteristics of the GaSe device on linear and log scale (the small current glitch at $V_{gs} \approx$ 10 *V* and $V_{gs} \approx$ 40 *V* is an instrumental effect), c) I_{on} current, and d) hysteresis width at different V_{ds}.

few-layer and enhances the responsivity of the device. **Figure 6**a,b illustrates the transfer characteristics of the transistor under ambient pressure and at room temperature, both in the dark and under a white laser source exposure, on linear and log scales. A photocurrent is seen in the off state when the dark current of the device in below 1 μA. In the on-state, the dark current of the device rises above the μA and the photocurrent becomes comparatively negligible. When illuminated, the transistor experiences an appreciable reduction in the threshold voltage and a left-shift in the transfer characteristic. The left-shift of the transfer curve under illumination is ascribed to the trapped holes that induce an increased electron concentration and a subsequent decrease in the threshold voltage, ultimately enhancing the transistor's conductivity. This so-called photogating effect, attributed to charge trapping at the interface with SiO_2 and in channel intrinsic defects, is quite common in 2D materials-based transistors.[57–60] A detailed description of transfer characteristics under laser exposure at different V_{ds} is reported in Figure S1 (Supporting Information), where it is confirmed the enhanced performance of the GaSe device under ambient conditions (see Figure S1, Supporting Information).

Further, we examine the transient behavior, i.e., the current–time characteristics, for different light incident powers. The measurements were carried out using a white laser with a maximum laser incident power of 110 mWcm^{-2} in the ambient conditions. Figure 6c shows the drain current under the laser on and off conditions as a function of different laser incident power percentages for 30 s-long pulses. The device shows an increase in the current with increasing laser power at fixed V_{ds} = 200 mV, and V_{gs} = 0 V. When light is incident on the active area of the GaSe FET device, it generates electron–hole pairs that are subsequently separated by the drain bias, resulting in a photocurrent. Moreover, as the device is measured in ambient conditions, desorption of O_2 and H_2O molecules contributes to the photocurrent. The O_2 and H_2O molecules physisorbed on the GaSe surface are desorbed under light exposure leaving free electrons and thus increasing the n-doping of GaSe which increases the channel conductivity.[15,61] The photocurrent is calculated using the relation, $I_{ph} = I_{light} - I_{dark}$, where I_{light} and I_{dark} are the current under laser illumination and in dark conditions, respectively. Figure 6d demonstrates the corresponding linear dependence of the photocurrent on the laser power (from 20% to 100% of its maximum incident power, which is 110 mW cm^{-2}, with steps of 20%). The linear behavior suggests an ideal application of GaSe as a photodetector. Further, we evaluated the photo responsivity (R) of the device through the relation, $R = I_{ph}/P_{inc}$, where I_{ph} is the calculated photocurrent and P_{inc} is the laser power incident on the device area, 300 μm^2. The highest responsivity obtained was about, $R \approx$475 mAW^{-1}, see Figure 6e. Similarly, photosensitivity (S) indicates the conductivity produced by light exposure over a certain bias voltage at a given incident laser power. The sensitivity (S) of the GaSe flake with thickness (d) = 100 nm at V_{ds} = 200 mV was calculated using the following equation:

$$S = \frac{R \times d}{V_{ds}} \quad (2)$$

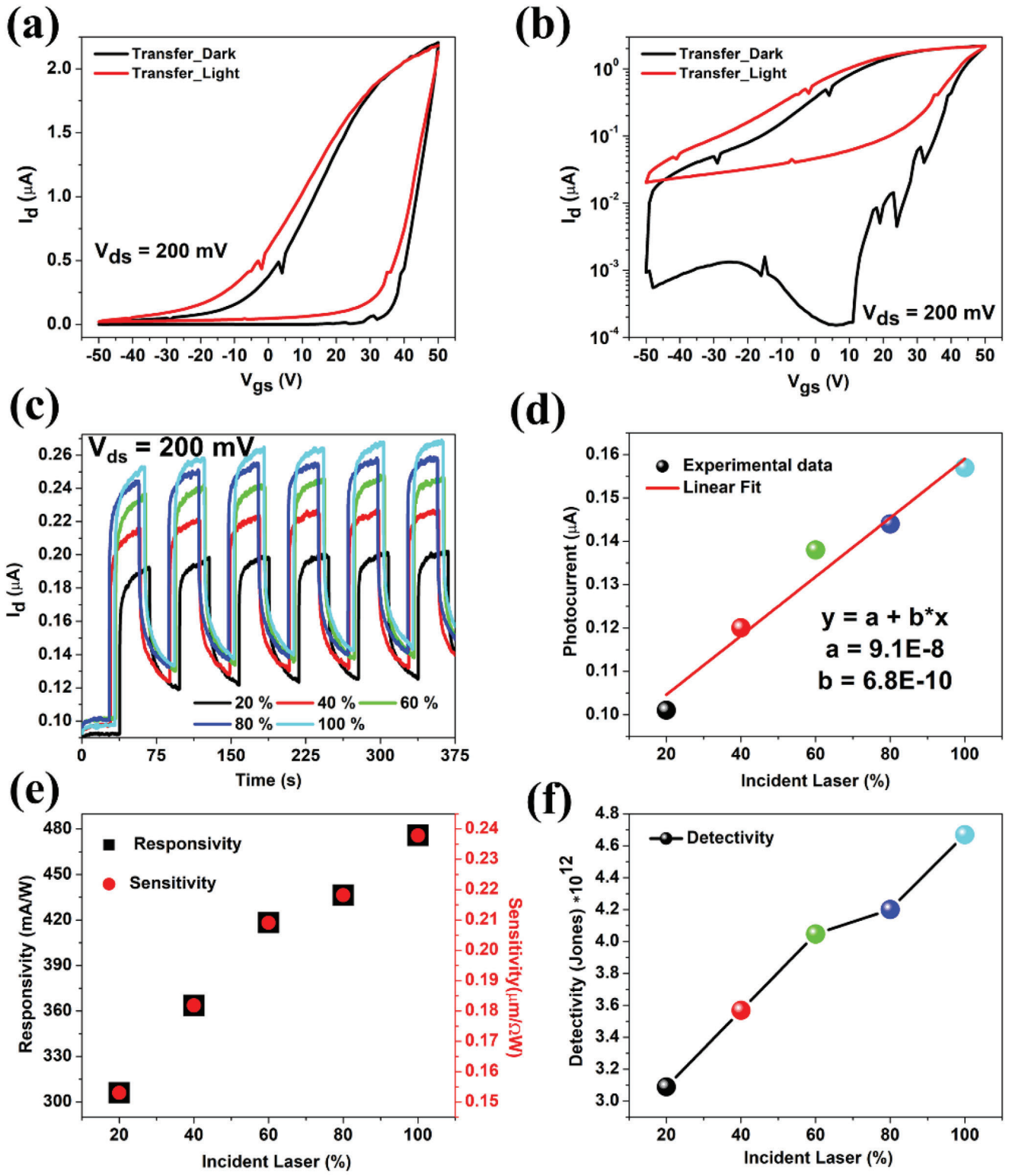

Figure 6. Transfer characteristics measured in light and dark conditions on a) linear and b) log scale, c) current in the forward bias under light illumination, at V_{ds} = 200 mV and V_{gs} = 0 V, d) photocurrent, e) responsivity, sensitivity, and f) detectivity, at various laser incident power percentages.

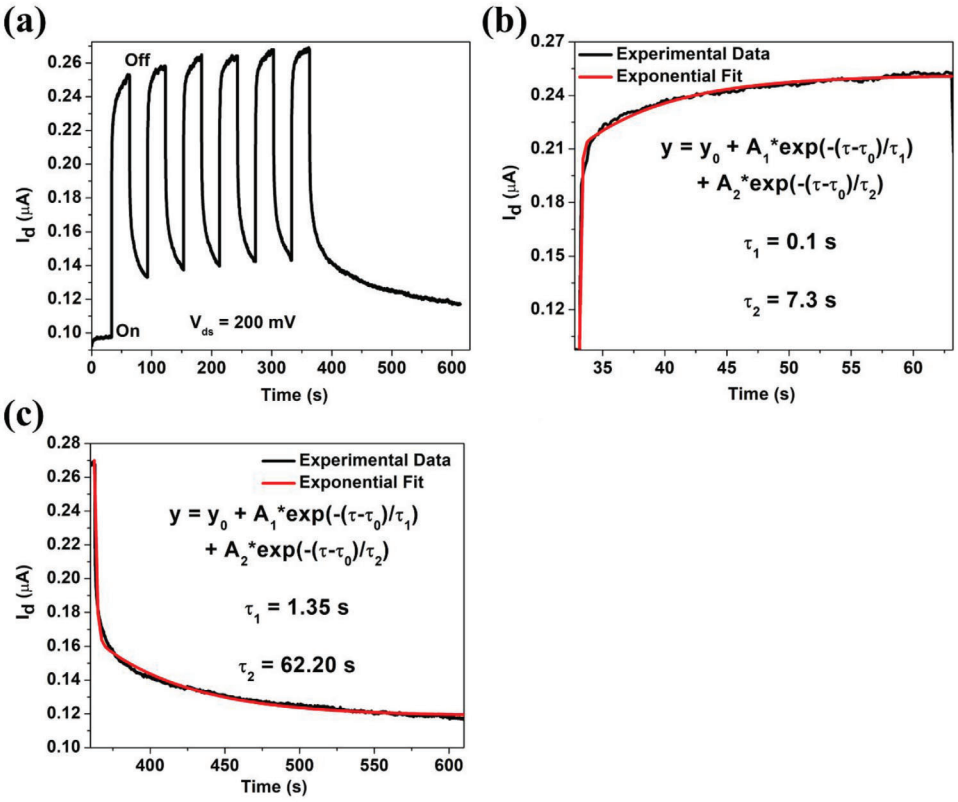

Figure 7. a) Current pulses under maximum incident power in dark-light-dark conditions, b) exponential rise fit of the initial rise pulse, and c) decay fit of the last pulse.

The maximum calculated sensitivity of the GaSe device is 0.24 μmΩW^{-1}, as shown in Figure 6e.

Further, from the experimental data, we calculated the detectivity (D) of the fabricated GaSe device, where D is defined as

$$D = \frac{\sqrt{S}R}{\sqrt{2eI_{dark}}} \tag{3}$$

where e is the electron charge. The calculated detectivity for the 300 μm^2 GaSe channel is ≈4.6 × 10^{12} Jones at ambient conditions, see Figure 6f. The obtained detectivity is comparable or even superior to the previously reported literature.[29,62,63] The high value of photo responsivity and detectivity could be due to the thick effective absorption layer.

To evaluate the optical response time of the GaSe device, a pulse train was applied using the laser light source set at its maximum power. The response time was analyzed considering the first and the last pulse of the photocurrent form, at V_{ds} = 200 mV, as shown in **Figure** 7a. The rise and decay in photocurrent in response to the laser light illumination on the photodetector presents a double exponential rise/decay and is expressed mathematically by the following empirical equation:

$$y = y_0 + A_1 \times \exp\left(-\frac{(\tau - \tau_0)}{\tau_1}\right) + A_2 \times \exp\left(-\frac{\tau - \tau_0}{\tau_2}\right) \tag{4}$$

where y_0 is the current at the steady state, A_1 and A_2 are the scaling factors, τ_1 and τ_2 are the time constants, and τ is the time. As can be seen in **Figure** 7, the photocurrent initially increases sharply due to carrier photogeneration with a time constant lower than τ_1 = 0.1 s (limited by the sensitivity of the experimental setup), followed by a slow rise later with the time constant τ_2 = 7.3 s due to slow photogating effect and desorption of adsorbates (see Figure 7b).[61,64] When the laser light is turned off, the photocurrent also shows two regimes, a sharp fall followed by a relatively slower decay (Figure 7c), with double time constants τ_1 = 1.3 s and τ_2 = 62.2 s, due to electron–hole pairs recombination and charge trapping at GaSe–SiO_2 interface as well as reabsorption of O_2 and H_2O molecules onto the GaSe surface.[61] Table S1 (Supporting Information) shows the comparison of figures of merit of GaSe and some other 2D materials-based photodetectors.

Further, the fabricated GaSe device was investigated for memory applications. We explored the GaSe device with the influence of light stimuli for optoelectronic memory. **Figure** 8a shows the performance of the device measured over a series of $V_{gs} = \pm 50$ V pulses, while the I_d current is recorded over time, at ambient conditions and a fixed V_{ds} = 200 mV. The device shows stable memory performance for more than 1 h, with two current levels, ON and OFF separated by gate pulses, similar to other 2D materials-based memories with charge trapping layers.[65] When the gate pulse is in the high positive (negative) state, the channel current increases (decreases) rapidly, and the charges get trapped in or

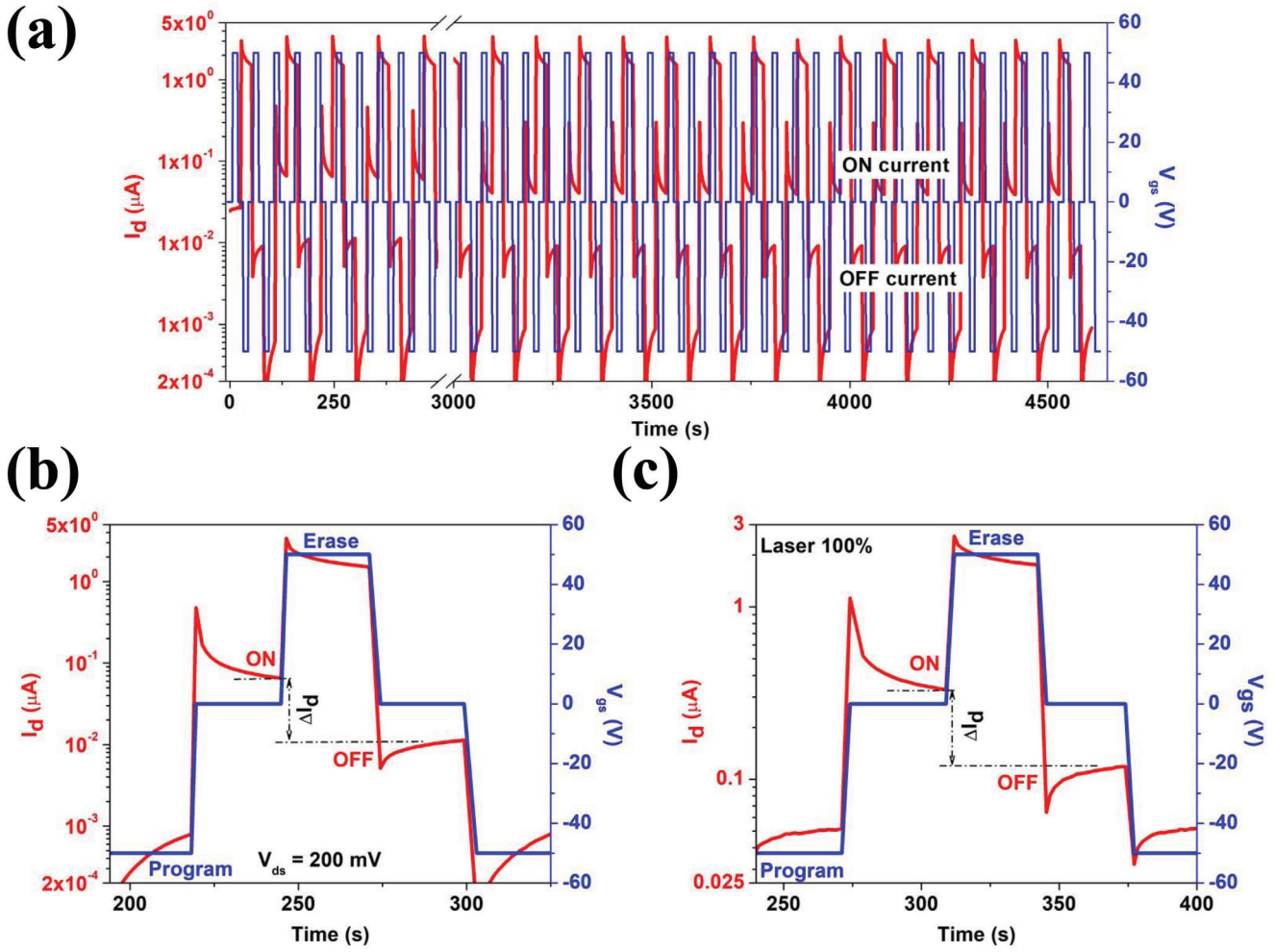

Figure 8. a) Channel current (red line) recorded under gate pulses (blue line) at ± 50 V showing repeated cycles, single program–erase cycle b) under dark, and c) under maximum laser power.

emitted from the trap states. After that, two states with different current values can be defined at $V_{gs} = \pm 0$ V, corresponding to the ON and the OFF state of a memory device, respectively[66] (see Figure 8b). Figure 8c shows that the exposure to light substantially increases the separation between the ON and OFF states. The two states are separated by ≈2 orders of magnitude under laser exposure, while the memory window (ΔI_d) is quadrupled in comparison to the dark. The results that represent a major contribution of this work, were expected as the laser light illumination causes both the generation of electron–hole pairs as well as the excitation of trapped charges, which increase the carrier concentration in the GaSe channel. These carriers can alter the local charge distribution, lowering the barrier height, hence exponential increase in current.[67] Charges excited from the trap states induce an increase in the photocurrent.

Concisely, the optical memory functions by originating charge-trapping sites for light-generated charge carriers, allowing them to be retained with persistence even after the light source is removed. This enables the storage of optical information within the memory. Additionally, the photocurrent reveals that the quantity of light-generated charge carriers is dictated by the intensity of light, typically associated with charge trapping or interfacial states. Consequently, adjusting the light intensity could offer a path to attain multiple memory states.

3. Conclusion

In summary, we fabricated a FET with mechanically exfoliated 100 nm thick GaSe flake showing n-type conduction. Our DFT simulations suggested the reason for electron transport to be due to the smaller conduction band offset compared to the valence band offset at the GaSe–Ni interface. The transfer characteristics of the FET device exhibit hysteresis that is modulated by the gate and the drain bias as a contribution of both extrinsic and intrinsic trap states. The back-gated FET showed wider hysteresis at higher applied gate voltage and a high I_{on} and I_{off} ratio of 10^3. The fabricated GaSe FET exhibits high field effect mobility up to 28 $cm^2\ V^{-1}\ s^{-1}$ at ambient conditions. Further, a decrease in the threshold voltage and the left-shift of the transfer characteristic with a slight increase in the current were also observed. The device shows a photo response of about 475 mAW^{-1} and a high detectivity of 4.6×10^{12} Jones under the illumination of maximum

laser power. It has been shown that the time-resolved photocurrent exhibits a fast rise and decay time of 0.1 and 1.3 s, respectively, followed by a slow rise and decay time of several seconds, respectively. In addition, the device showed memory behavior with measured stability of more than 1 h with repeatable cycles and sensitive to the light stimuli confirming the nonvolatile optoelectronic memory with an enhanced programming window of 2 orders of magnitude. The results provide better understanding of GaSe thin flake and demonstrate that the investigated material could be a suitable material for future electronic and optical devices.

4. Experimental Section

A bulk GaSe single crystal was used to perform mechanical exfoliation, resulting in the production of GaSe thin flakes using Scotch tape. These exfoliated flakes were subsequently transferred onto a substrate consisting of 300 nm thick SiO_2/p+ Si (consistent with the schematic reported in Figure 1d). Metal contacts were defined using standard photolithography and lift-off process to define 15/150 nm Ni/Au metal contact. The AFM image of GaSe flake was acquired by using a Nanosurf A.G. microscope. The micro-Raman measurements were carried out using a commercial inVia Renishaw Raman microscope with a 20× objective and Centrus CCD detector. The Raman spectra measurements were performed using a 514 nm laser at room temperature.

To get insight into the atomistic structure and electrical characteristics of GaSe in contact with Ni metal, DFT and nonequilibrium Green's function NEGF have been carried out as implemented in QuantumATK.[68] Linear combination of numerical atomic-orbital basis set and generalized gradient approximation GGA norm-conserving pseudopotentials from PseudoDojo with medium basis sets[69] are employed in the simulations. Brillouin zone integrations are performed over a grid of k-points generated according to the Monkhorst–Pack scheme,[70] with a density of approximately 10 k-points per angstrom. An energy cut-off of 120 Ha and energy convergence criterion of 10^{-6} Ha have also been considered. For the discretized grid, ≈620 k-point per angstrom have been used for the Green's function calculations, in the direction normal to the metal–GaSe interface plane. Structural relaxation is performed with a maximum force of less than 0.02 eV $Å^{-1}$. The metal crystallographic orientation with a common supercell with minimal strain for Ni [111] has been considered with 1.5% strain. The strain arising from the lattice constant mismatch between the materials at the Ni–GaSe interface has been applied to the metal electrodes, since, unlike GaSe, a few percent in-plane lattice constant of metal surface does not affect its electronic properties considerably.[71] Continuous doping models with electron modification per atom and adding a neutralizing compensation charge to the atomic charge have been considered as dopant profiles.[72]

The electrical measurements were performed on a probe station (Lake Shore Cryotronics, Inc.) endowed with four metallic nanoprobes, connected to a Keithley 4200 semiconductor characterization system (Tektronix Inc.), and one additional probe with optical fiber to control the position of a light beam inside the chamber. The optoelectronic measurements were investigated under illumination by a supercontinuum white laser (SuperK COMPACT by NKT Photonics) with a maximum incident power of 110 $mWcm^{-2}$. All electrical measurements were performed in a two-probe configuration at ambient conditions.

Supporting Information

Supporting Information is available from the Wiley Online Library or from the author.

Acknowledgements

A.D.B. and A.K. acknowledge the financial support from the European Union's REACT-EU PON Research and Innovation 2014–2020, Ministerial Decree 1062/2021. H.N., V.P., L.A., P.K.H. and F.G. acknowledge the financial support from Science Foundation Ireland AMBER Research Centre (SFI-12/RC/2278_P2). The SFI/HEA Irish Centre for High-End Computing (ICHEC) is acknowledged for the provision of computational facilities and support.

Conflict of Interest

The authors declare no conflict of interest.

Author Contributions

The manuscript was written through the contributions of all authors. All authors have approved the final version of the manuscript.

Data Availability Statement

The data that support the findings of this study are available from the corresponding author upon reasonable request.

Keywords

2D materials, density functional theory, field effect transistor, GaSe, optoelectronic memory, photodetector

Received: January 9, 2024
Revised: February 9, 2024
Published online: April 4, 2024

[1] M. Xu, T. Liang, M. Shi, H. Chen, *Chem. Rev.* **2013**, *113*, 3766.
[2] A. Di Bartolomeo, *Nanomaterials* **2020**, *10*, 579.
[3] F. Urban, G. Lupina, A. Grillo, N. Martucciello, A. Di Bartolomeo, *Nano Ex* **2020**, *1*, 010001.
[4] S. Tajik, Z. Dourandish, F. Garkani Nejad, H. Beitollahi, P. M. Jahani, A. Di Bartolomeo, *Biosens. Bioelectron.* **2022**, *216*, 114674.
[5] M. B. Askari, P. Salarizadeh, P. Veisi, E. Samiei, H. Saeidfirozeh, M. T. Tourchi Moghadam, A. Di Bartolomeo, *Micromachines* **2023**, *14*, 691.
[6] X. Duan, C. Wang, A. Pan, R. Yu, X. Duan, *Chem. Soc. Rev.* **2015**, *44*, 8859.
[7] L. Iemmo, A. Di Bartolomeo, F. Giubileo, G. Luongo, M. Passacantando, G. Niu, F. Hatami, O. Skibitzki, T. Schroeder, *Nanotechnology* **2017**, *28*, 495705.
[8] F. Bonaccorso, Z. Sun, T. Hasan, A. C. Ferrari, *Nature Photon* **2010**, *4*, 611.
[9] A. Pelella, A. Grillo, E. Faella, G. Luongo, M. B. Askari, A. Di Bartolomeo, *ACS Appl. Mater. Interfaces* **2021**, *13*, 47895.
[10] A. Grillo, M. Passacantando, A. Zak, A. Pelella, A. Di Bartolomeo, *Small* **2020**, *16*, 2002880.
[11] O. Durante, K. Intonti, L. Viscardi, S. De Stefano, E. Faella, A. Kumar, A. Pelella, F. Romeo, F. Giubileo, M. S. G. Alghamdi, M. A. S. Alshehri, M. F. Craciun, S. Russo, A. Di Bartolomeo, *ACS Appl. Nano Mater* **2023**, *6*, 21663.
[12] A. Kumar, L. Viscardi, E. Faella, F. Giubileo, K. Intonti, A. Pelella, S. Sleziona, O. Kharsah, M. Schleberger, A. Di Bartolomeo, *J. Mater. Sci.* **2023**, *58*, 2689.
[13] M. Amani, M. L. Chin, A. G. Birdwell, O'T. P. Regan, S. Najmaei, Z. Liu, P. M. Ajayan, J. Lou, M. Dubey, *Appl. Phys. Lett.* **2013**, *102*, 193107.
[14] A. Di Bartolomeo, F. Urban, M. Passacantando, N. McEvoy, L. Peters, L. Iemmo, G. Luongo, F. Romeo, F. Giubileo, *Nanoscale* **2019**, *11*, 1538.

[15] A. Grillo, E. Faella, A. Pelella, F. Giubileo, L. Ansari, F. Gity, P. K. Hurley, N. McEvoy, B. Di, *Adv. Funct. Mater.* **2021**, *31*, 2105722.
[16] K. Intonti, E. Faella, L. Viscardi, A. Kumar, O. Durante, F. Giubileo, M. Passacantando, H. T. Lam, K. Anastasiou, M. F. Craciun, S. Russo, A. Di Bartolomeo, *Ad. Electr. Mater.* **2023**, *9*, 2300066.
[17] A. Pelella, K. Intonti, L. Viscardi, O. Durante, D. Capista, M. Passacantando, F. Giubileo, P. Romano, M. A. S. Alshehri, M. S. G. Alghamdi, M. F. Craciun, S. Russo, A. Di Bartolomeo, *J. Phys. Chem. Solids* **2023**, *183*, 111653.
[18] A. Kumar, E. Faella, O. Durante, F. Giubileo, A. Pelella, L. Viscardi, K. Intonti, S. Sleziona, M. Schleberger, B. Di, *J. Phys. Chem. Solids* **2023**, *179*, 111406,.
[19] D. Xiang, T. Liu, J. Xu, J. Y. Tan, Z. Hu, B. Lei, Y. Zheng, J. Wu, A. H. C. Neto, L. Liu, W. Chen, *Nat Commun* **2018**, *9*, 2966.
[20] F. Zhou, J. Chen, X. Tao, X. Wang, Y. Chai, *Research* **2019**, *2019*, 9490413.
[21] A. Kumar, L. Viscardi, E. Faella, F. Giubileo, K. Intonti, A. Pelella, S. Sleziona, O. Kharsah, M. Schleberger, A. Di Bartolomeo, *Nano Ex* **2023**, *4*, 014001.
[22] E. Faella, K. Intonti, L. Viscardi, F. Giubileo, A. Kumar, H. T. Lam, K. Anastasiou, M. F. Craciun, S. Russo, A. Di Bartolomeo, *Nanomaterials* **2022**, *12*, 1886.
[23] L. Kou, T. Frauenheim, C. Chen, *J. Phys. Chem. Lett.* **2014**, *5*, 2675.
[24] J. Guo, Y. Liu, Y. Ma, E. Zhu, S. Lee, Z. Lu, Z. Zhao, C. Xu, S.-J. Lee, H. Wu, K. Kovnir, Y. Huang, X. Duan, *Adv. Mater.* **2018**, *30*, 1705934.
[25] A. S. Sarkar, E. Stratakis, *Adv. Sci.* **2020**, *7*, 2001655.
[26] A. Di Bartolomeo, A. Grillo, F. Giubileo, L. Camilli, J. Sun, D. Capista, M. Passacantando, *J. Phys. D: Appl. Phys.* **2021**, *54*, 105302.
[27] J. Sun, M. Passacantando, M. Palummo, M. Nardone, K. Kaasbjerg, A. Grillo, A. Di Bartolomeo, J. M. Caridad, L. Camilli, *Phys. Rev. Applied* **2020**, *13*, 044063.
[28] A. Grillo, A. Di Bartolomeo, F. Urban, M. Passacantando, J. M. Caridad, J. Sun, L. Camilli, *ACS Appl. Mater. Interfaces* **2020**, *12*, 12998.
[29] S. Sorifi, S. Kaushik, R. Singh, *Nanoscale Adv.* **2022**, *4*, 479.
[30] P. Hauchecorne, F. Gity, M. Martin, H. Okuno, S. Bhattacharjee, J. Moeyaert, D. Rouchon, B. Hyot, P. K. Hurley, T. Baron, *ACS Appl. Nano Mater.* **2021**, *4*, 7820.
[31] D. V. Rybkovskiy, N. R. Arutyunyan, A. S. Orekhov, I. A. Gromchenko, I. V. Vorobiev, A. V. Osadchy, E. Y. Salaev, T. K. Baykara, K. R. Allakhverdiev, E. D. Obraztsova, *Phys. Rev. B* **2011**, *84*, 085314.
[32] A. Kuhn, A. Chevy, R. Chevalier, *physica status solidi (a)* **1975**, *31*, 469.
[33] Y. Cao, K. Cai, P. Hu, L. Zhao, T. Yan, W. Luo, X. Zhang, X. Wu, K. Wang, H. Zheng, *Sci Rep* **2015**, *5*, 8130.
[34] V. Augelli, C. Manfredotti, R. Murri, L. Vasanelli, *Phys. Rev. B* **1978**, *17*, 3221.
[35] X. Yuan, L. Tang, S. Liu, P. Wang, Z. Chen, C. Zhang, Y. Liu, W. Wang, Y. Zou, C. Liu, N. Guo, J. Zou, P. Zhou, W. Hu, F. Xiu, *Nano Lett.* **2015**, *15*, 3571.
[36] Y. Zhou, Y. Nie, Y. Liu, K. Yan, J. Hong, C. Jin, Y. Zhou, J. Yin, Z. Liu, H. Peng, *ACS Nano* **2014**, *8*, 1485.
[37] Y. Wu, D. Zhang, K. Lee, G. S. Duesberg, A. Syrlybekov, X. Liu, M. Abid, M. Abid, Y. Liu, L. Zhang, C. Ó. Coileáin, H. Xu, J. Cho, M. Choi, B. S. Chun, H. Wang, H. Liu, H.-C. Wu, *Adv. Mater. Technol.* **2017**, *2*, 1600197.
[38] Y.-F. Zhao, H.-R Fuh, C. Ó. Coileáin, C. P. Cullen, T. Stimpel-Lindner, G. S. Duesberg, Ó. Leonardo Camargo Moreira, D. Zhang, J. Cho, M. Choi, B. S. Chun, C.-R. Chang, H.-C. Wu, *Adv. Mater. Technol.* **2020**, *5*, 1901085.
[39] Z. B. Aziza, H. Henck, D. Pierucci, M. G. Silly, E. Lhuillier, G. Patriarche, F. Sirotti, M. Eddrief, A. Ouerghi, *ACS Nano* **2016**, *10*, 9679.
[40] S. Quan, Y. Wang, Y. Liang, J. Jiang, B. Zhong, K. Yu, H. Zhang, G. Kan, *J. Phys. Chem. C* **2020**, *124*, 10185.
[41] M. Bejani, O. Pulci, J. Barvestani, A. S. Vala, F. Bechstedt, E. Cannuccia, *Phys. Rev. Mater.* **2019**, *3*, 124003.
[42] A. Di Bartolomeo, A. Grillo, F. Urban, L. Iemmo, F. Giubileo, G. Luongo, G. Amato, L. Croin, L. Sun, S.-J. Liang, L. K. Ang, *Adv. Funct. Mater.* **2018**, *28*, 1800657.
[43] A. Grillo, A. Di Bartolomeo, *Adv. Electron. Mater.* **2021**, *7*, 2000979.
[44] N. Liu, S. Zhou, N. Gao, J. Zhao, *Phys. Chem. Chem. Phys.* **2018**, *20*, 21732.
[45] S. Sorifi, P. Aggarwal, S. Kaushik, R. Singh, *ACS Appl. Electron. Mater.* **2023**, *5*, 451.
[46] A. D. Bartolomeo, L. Genovese, F. Giubileo, L. Iemmo, G. Luongo, T. Foller, M. Schleberger, *2D Mater* **2017**, *5*, 015014.
[47] F. Urban, N. Martucciello, L. Peters, N. McEvoy, A. Di Bartolomeo, *Nanomaterials* **2018**, *8*, 901.
[48] J. Shu, G. Wu, Y. Guo, B. Liu, X. Wei, Q. Chen, *Nanoscale* **2016**, *8*, 3049.
[49] F. Urban, F. Giubileo, A. Grillo, L. Iemmo, G. Luongo, M. Passacantando, T. Foller, L. Madauß, E. Pollmann, M. P. Geller, D. Oing, M. Schleberger, A. Di Bartolomeo, *2D Mater* **2019**, *6*, 045049.
[50] C. Lee, S. Rathi, M. A. Khan, D. Lim, Y. Kim, S. J. Yun, D.-H. Youn, K. Watanabe, T. Taniguchi, G.-H. Kim, *Nanotechnology* **2018**, *29*, 335202.
[51] H. Huang, P. Wang, Y. Gao, X. Wang, T. Lin, J. Wang, L. Liao, J. Sun, X. Meng, Z. Huang, X. Chen, J. Chu, *Appl. Phys. Lett.* **2015**, *107*, 143112.
[52] A. Abderrahmane, P.-G. Jung, N.-H. Kim, P. J. Ko, A. Sandhu, *Opt. Mater. Express, OME* **2017**, *7*, 587.
[53] S. Yang, Q. Yue, H. Cai, K. Wu, C. Jiang, S. Tongay, *J. Mater. Chem. C* **2015**, *4*, 248.
[54] D. J. Late, B. Liu, J. Luo, A. Yan, H. S. S. R. Matte, M. Grayson, C. N. R. Rao, V. P. Dravid, *Adv. Mater.* **2012**, *24*, 3549,.
[55] R. Minder, G. Ottaviani, C. Canali, *J. Phys. Chem. Solids* **1976**, *37*, 417.
[56] J. C. Greer, A. Blom, L. Ansari, *J. Phys.: Condens. Matter* **2018**, *30*, 414003.
[57] A. Di Bartolomeo, L. Genovese, T. Foller, F. Giubileo, G. Luongo, L. Croin, S.-J. Liang, L. K. Ang, M. Schleberger, *Nanotechnology* **2017**, *28*, 214002.
[58] Y.-C. Wu, C.-H. Liu, S.-Y. Chen, F.-Y. Shih, P.-H. Ho, C.-W. Chen, C.-T. Liang, W.-H. Wang, *Sci Rep* **2015**, *5*, 11472.
[59] A. Di Bartolomeo, L. Iemmo, F. Giubileo, G. Luongo, F. Urban, A. Grillo, in *Proc. of the 2018 IEEE 13th Nanotechnology Materials and Devices Conference (NMDC)*, IEEE, Portland, OR, USA, **2018**, pp. 1–2.
[60] K. Intonti, E. Faella, A. Kumar, L. Viscardi, F. Giubileo, N. Martucciello, H. T. Lam, K. Anastasiou, M. Craciun, S. Russo, A. Di Bartolomeo, *ACS Appl. Mater. Interfaces* **2023**, *15*, 50302.
[61] A. Di Bartolomeo, A. Kumar, O. Durante, A. Sessa, E. Faella, L. Viscardi, K. Intonti, F. Giubileo, N. Martucciello, P. Romano, S. Sleziona, M. Schleberger, *Materials Today Nano* **2023**, *24*, 100382.
[62] S. Sorifi, M. Moun, S. Kaushik, R. Singh, *ACS Appl. Electron. Mater.* **2020**, *2*, 670.
[63] R. K. Saroj, P. Guha, S. Lee, D. Yoo, E. Lee, J. Lee, M. Kim, G.-C. Yi, *Adv. Opt. Mater.* **2022**, *10*, 2200332,.
[64] V. K. Pulikodan, A. Alexander, A. B. Pillai, M. A. Namboothiry, *ACS Appl. Nano Mater.* **2020**, *3*, 10057.
[65] A. Grillo, A. Pelella, E. Faella, F. Giubileo, S. Sleziona, O. Kharsah, M. Schleberger, A. Di Bartolomeo, *2D Mater* **2022**, *9*, 015028.
[66] A. Di Bartolomeo, Y. Yang, M. B. M. Rinzan, A. K. Boyd, P. Barbara, *Nanoscale Res. Lett.* **2010**, *5*, 1852.
[67] M.-Y. Lu, M.-P. Lu, S.-J. You, C.-W. Chen, Y.-J. Wang, *Sci. Rep.* **2015**, *5*, 15123.
[68] Atomistic Simulation Software | QuantumATK – Synopsys Available online, https://www.synopsys.com/manufacturing/quantumatk.html, (accessed: December, 2023).

[69] M. J. van Setten, M. Giantomassi, E. Bousquet, M. J. Verstraete, D. R. Hamann, X. Gonze, G.-M. Rignanese, *Comput. Phys. Commun.* **2018**, *226*, 39.
[70] H. J. Monkhorst, J. D. Pack, *Phys. Rev. B* **1976**, *13*, 5188.
[71] M. Bokdam, G. Brocks, M. I. Katsnelson, P. J. Kelly, *Phys. Rev. B* **2014**, *90*, 085415.
[72] D. Stradi, U. Martinez, A. Blom, M. Brandbyge, K. Stokbro, *Phys. Rev. B* **2016**, *93*, 155302.